

An Exploratory Study to Derive Precipitation over Land from X-Band Synthetic Aperture Radar Measurements

J. A. WEINMAN

Department of Atmospheric Sciences, University of Washington, Seattle, Washington

F. S. MARZANO

Department of Electronic Engineering, University of Rome, La Sapienza, Rome, and CETEMPS, University of L'Aquila, L'Aquila, Italy

(Manuscript received 8 December 2006, in final form 16 May 2007)

ABSTRACT

Global precipitation measurements from space-based radars and microwave radiometers have been the subject of numerous studies during the past decade. Rainfall retrievals over land from spaceborne microwave radiometers depend mainly on scattering from frozen hydrometeors. Unfortunately, the relationship between frozen hydrometeors and rainfall varies considerably. The large field of view and related beam filling of microwave radiometer footprints introduce additional difficulties. Some of these problems will be addressed by the improved sensors that will be placed on the Global Precipitation Measurement (GPM) core satellite. Two shuttle missions demonstrated that X-band synthetic aperture radar (X-SAR) could observe rainfall over land. Several X-band SARs that can provide such measurements will be launched in the coming decade. These include four Constellation of Small Satellites for Mediterranean Basin Observations (COSMO-SkyMed), two TerraSAR-X, and a fifth Korea Multipurpose Satellite (KOMPSAT-5) to be launched by the Italian, German, and Korean Space Agencies, respectively. Data from these satellites could augment the information available to the GPM science community. The present study presents computations of normalized radar cross sections (NRCS) that employed a simple, idealized two-layer cloud model that contained both rain and frozen hydrometeors. The modeled spatial distributions of these hydrometeors varied with height and horizontal distance. An exploratory algorithm was developed to retrieve the shape, width, and simple representations of the vertical profiles of frozen hydrometeors and rain from modeled NRCS scans. A discussion of uncertainties in the retrieval is presented.

1. Introduction

Precipitation has a profound influence on a broad range of human activity. Measurement of global precipitation is thus a major goal of climate and hydrological investigations. Numerous studies conducted as part of the Tropical Rainfall Measuring Mission (TRMM) program have demonstrated the benefits of spaceborne precipitation measurements toward achieving a better understanding of the global hydrological cycle. A description of the TRMM and some scientific results that

have been obtained from TRMM can be found in Kummerow et al. (2000).

The National Aeronautics and Space Administration (NASA) Global Precipitation Mission (GPM) is an outgrowth of TRMM that will improve precipitation measurements and extend those measurements to higher latitudes. The GPM core satellite will carry a 13.4-GHz scanning radar and a 35.6-GHz nadir staring radar, as well as an improved microwave radiometer. Additional data will be acquired from microwave radiometers that will be carried by a constellation of satellites that expand the coverage provided by the core satellite.

Spaceborne microwave radiometers have had limited success in retrieving precipitation over land because they rely heavily on the scattering properties of ice in the upper regions of precipitating clouds. Bennartz and

Corresponding author address: James Weinman, Department of Atmospheric Sciences, University of Washington, Box 351640, Seattle, WA 98195-1640.
E-mail: weinman@atmos.washington.edu

TABLE 1. System parameters of forthcoming X-SAR satellite systems. Note that H stands for horizontal and V stands for vertical polarization. For more general information see also <http://www.asi.it> for CSM, <http://www.dlr.de/tsx> for *TSX*, and <http://www.kari.re.kr/> for KOMPSAT-5.

	Wavelength (cm)	Polarization capability	ScanSAR swath width (km)	ScanSAR resolution (m)	Orbit altitude (km)	Incidence angle range (°)	Mission duration (yr)
CSM	3.1 (X band)	HH, VV selectable	200	30–100	620	25–57	5
<i>TSX</i>	3.1 (X band)	HH, HV, VH, VV	100	16	514	20–45	5
KOMPSAT-5	3.1 (X band)	HH, HV, VH, VV	100	16	514	20–45	5

Petty (2001) showed that those scattering properties may at times be poorly related to surface rainfall rates. Beam filling has also limited the efficacy of rainfall retrievals from passive radiometry (e.g., Kummerow 1998).

Atlas and Moore (1987) showed that precipitation distributions could be derived from normalized radar cross sections (NRCS) using the real aperture radar equation. Mean rainfall rates were previously derived from X-band synthetic aperture radar (X-SAR) measurements by Jameson et al. (1997), Moore et al. (1997), and Melsheimer et al. (1998). X-SAR precipitation retrievals may help to overcome some of the limitations of microwave radiometric precipitation retrievals cited above. Rainfall retrievals from X-SAR data will be especially valuable over mountainous terrain where the observing capability of ground- and space-based radars is limited. It should also be noted that the spatial resolution of weather forecast models is increasing so that precipitation distributions will also require the improved resolution that X-SARs can provide.

The hydrometeorological community will be able to benefit from two currently operating satellite missions. The *TerraSAR-X* (*TSX*) was launched on 15 June 2007 by the Deutsches Zentrum für Luft- und Raumfahrt (DLR). An overview of *TSX* is presented, for example, by Buckreuss et al. (2003) and Schwerdt et al. (2005). The *TSX* will be followed by a Tandem-X satellite that will be used for interferometric studies. It will be launched a year later (e.g., Weber and Hörmann 2006). The first of four satellites composing the Constellation of Small Satellites for Mediterranean Basin Observations (COSMO-SkyMed or CSM) was launched by the Agenzia Spaziale Italiana (ASI) on 8 June 2007. Descriptions of the four-satellite COSMO-SkyMed constellation can be found, for example, in Caltagirone et al. (2007) and Verdone et al. (2002). The Korea Aerospace Research Institute (KARI) also has plans to launch the fifth Korea Multipurpose Satellite (KOMPSAT-5) later in this decade. The KOMPSAT-5 specifications appear to be similar to those of *TSX*. A concise summary of some characteristics of these X-

SAR systems is presented in Table 1. It is worth noting that a SAR may operate in different modes and the spatial resolution usually is mode dependent. For instance, *TSX* exhibits the “Spotlight” mode with 10 km × 10 km scenes at a resolution of 1–2 m, the “Stripmap” mode with 30-km-wide strips at a resolution between 3 and 6 m, and the Scanning SAR (“ScanSAR”) mode with 100-km-wide strips at a resolution of 16 m.

Some aspects of X-SAR rain measurements may be summarized as follows: 1) Unlike the TRMM precipitation radar (PR), which provides highly resolved vertical precipitation profiles, X-SARs mainly measure the slant-path integrated scattering and attenuation of precipitation. However, unlike microwave radiometers, contrast between rain and land background signals is sufficient to measure terrestrial rainfall. 2) Beam filling has introduced ambiguities in precipitation estimates derived from microwave radiometry. The spatial resolution of X-SARs operating in a ScanSAR mode is better than a few hundreds of meters, even in rain (Atlas and Moore 1987). Much smaller rain cells can thus be observed. 3) Precipitation in mountainous terrain can cause flash floods, mud slides, and trigger avalanches. Mountainous terrain has presented challenges to both ground-based radars and the PR. Radar reflectivity measurements from PR are routinely removed within ~1–2 km of mountainous surfaces to avoid ground clutter. Partial beam filling by convective cells, whose width is comparable or less than 4 km, also adversely affects the response of the PR (Durden et al. 1998). The 23-dBZ noise floor of the PR limits the response of the PR to intense convective cells. The improved horizontal resolution of the X-SARs may overcome these limitations.

Marine precipitation has been observed by previous spaceborne X-SARs. Because it is difficult to separate the effects of downbursts, wind roughening, and rain impact on sea surfaces from those produced by precipitation, maritime rainfall will not be considered in this study.

The aim of this work is to provide a simple theoretical framework to model the X-SAR response due to

rainfall over land. In section 2, we will present an example of a previous X-SAR observation of rainfall over land, giving a qualitative description of the measured features. In section 3, an electromagnetic model of the NRCS will be introduced. Section 4 will describe an idealized model of the 2D distribution of hydrometeors used to compute NRCSs. In section 5, a prototype of a retrieval algorithm will be described. Section 6 will present an evaluation of the performance of the retrieval algorithm and errors in the retrieved spatial distributions of precipitation. Conclusions will be presented in section 7.

2. Example of X-SAR observation of rainfall

We will approach the problem of X-SAR precipitation retrieval by modeling the NRCS and qualitatively comparing model results with measurements obtained from the shuttle missions STS-59 and -68 of 1994. These missions employed an X-band SAR from the DLR along with L- and C-band SARs provided by the Jet Propulsion Laboratory (JPL) of the California Institute of Technology. The X-SAR operated with a swath width ~ 50 km with ~ 0.03 -km horizontal resolution in a ScanSAR mode. The X-SAR measured the NRCS produced by precipitation, with VV polarization (Jordan et al. 1995). Contrast between rain and land background signals was sufficient to permit the measurement of rainfall (Jameson et al. 1997; Moore et al. 1997; Mel-sheimer et al. 1998).

An example of such observations near Noakhali, Bangladesh, is shown in Fig. 1. Figure 1a shows a scene without precipitation. Figure 1b shows the same scene, but with a convective system in the right-hand side that affected the NRCS by approximately -3 to -30 dB. Note that a plume appears to be sheared nearly across the observed swath in the direction of the X-SAR satellite orbit at the top of the image. (Because this is an X-band image, this is not a simple cirrus anvil; the frozen particles are snow or graupel.) We will show that such an effect is just a manifestation of the oblique observation of a vertical column of frozen hydrometeors. The lower left-hand part of the image shows a dark region with negligible brightening toward the top. Our model suggests that such an effect could be produced by shallow rain in which liquid hydrometeors scatter little radiation, yet they absorb radiation on its way to and from the surface. One should be wary, however, because it is possible that this effect may be caused by surface wetting from an antecedent storm or it may be an artifact produced by anomalous transmission through the ionosphere or atmosphere.

3. Normalized radar cross-section model

The power received from a precipitating cell that is measured from a spaceborne SAR is the sum of two components: 1) the signal scattered by the underlying surface that is attenuated along the two-way slant path down to the surface and 2) the signal scattered by a volume along the wave front containing precipitation subjected to the two-way attenuation between the radar and the volume. In the following we will model NRCSs, indicated by σ_{SAR} , for a 2D atmospheric geometry in the x - z plane, where x is the cross-track coordinate that increases away from the satellite orbit, z is the height coordinate, and y is the along-orbit coordinate. The incident angle of slant SAR view is indicated by θ .

a. The radar equation for the NRCS

Figure 2 presents a schematic illustration of the radar reflectivity model that is considered. Microwave pulses emitted by the radar are approximated by plane wave front slices, shown as a pair of dashed lines separated by a width, Δr (see the appendix for a general treatment of the spherical wave front case). As we move from left to right, any slice that occurs to the left of the image is unaffected by the precipitation. Only σ^0 from the ground is measured. The height of the top of the frozen hydrometeor layer is z_t and the height of the freezing layer is z_0 . The width of the cell is w .

A slice at $0 \leq x \leq [(z_t - z_0)/\tan(\theta)]$ generally has an enhanced NRCS because scattering from the frozen precipitation is added to the return from the surface and attenuation is weak. For $[(z_t - z_0)/\tan(\theta)] \leq x \leq [z_t/\tan(\theta)]$, the NRCS is still enhanced, but attenuation in the liquid layer begins to reduce the NRCS. For $[z_t/\tan(\theta)] \leq x \leq [z_t/\tan(\theta) + w]$, the NRCS is generated within the precipitating cloud where scattering is both by the liquid and frozen hydrometeors and the underlying surface. The two-way attenuation by the liquid hydrometeors strongly reduces the NRCS as we move to the right. As we emerge from the precipitating cloud at $[z_t/\tan(\theta) + w] \leq x \leq [z_t [1/\tan(\theta) + \tan(\theta)] + w]$, the two-way attenuation of the signal reflected by the underlying surface diminishes so that the NRCS starts to increase. The NRCS finally returns to the background value at $x > x_{\text{max}}$, where $x_{\text{max}} = z_t [1/\tan(\theta) + \tan(\theta)] + w$.

Confining our attention to the cross-track geometry in the x - z plane, the NRCS, σ_{SAR} , consists of scattering from the surface, σ_{srf} , and scattering by the precipitation, σ_{vol} , such that

$$\sigma_{\text{SAR}} = \sigma_{\text{srf}} + \sigma_{\text{vol}}, \quad (1a)$$

where

$$\sigma_{\text{srf}} = \sigma^0 e^{-2} \int_0^{\infty} k[x(z)] dz / \cos\theta \quad (1b)$$

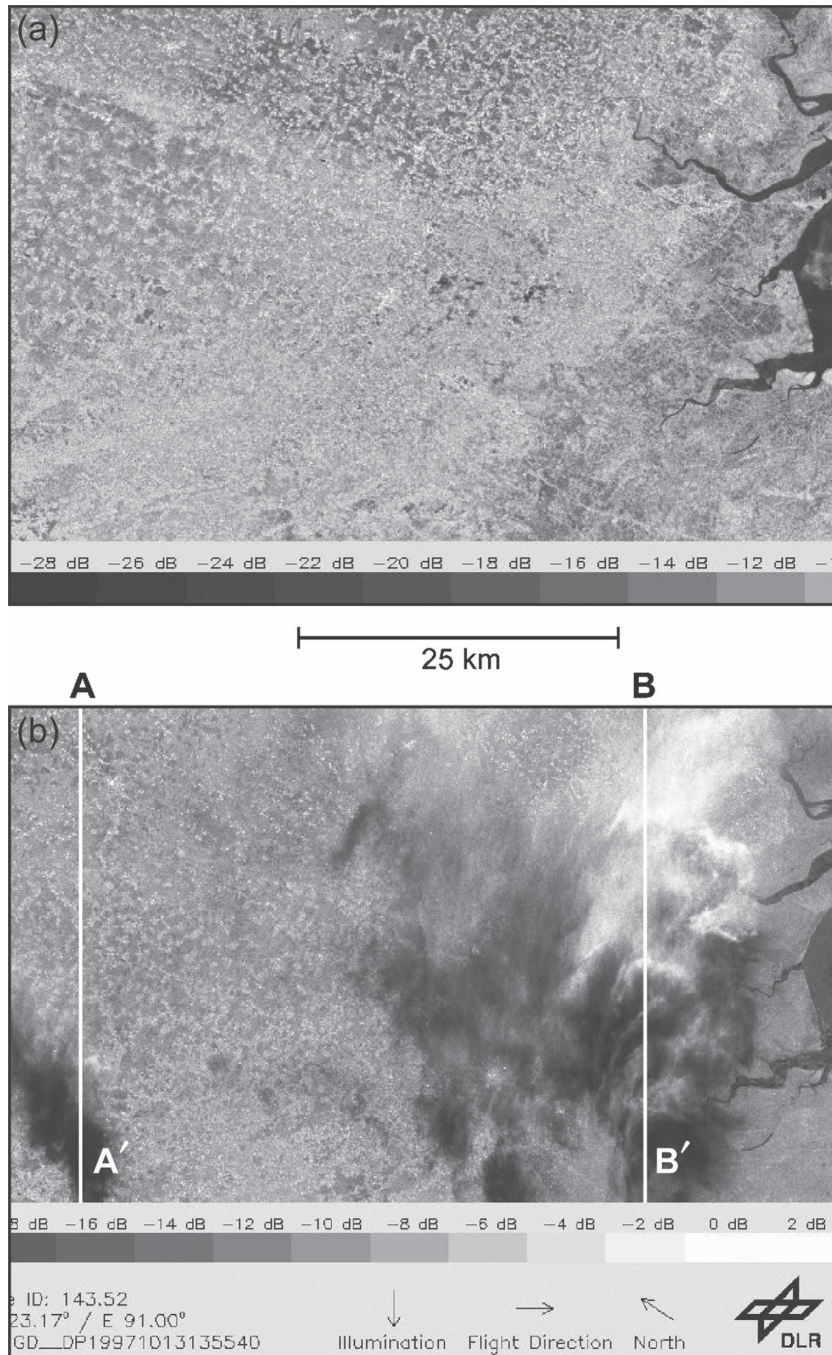


FIG. 1. (a) View around Noakhali, Bangladesh (22.8°N, 91.2°E), on 7 Oct 1994. (b) Same scene on 18 Apr 1994. Note scattering by frozen hydrometeors in the upper right, scattering and attenuation by rain in middle-lower right, and absorption mainly by rain only in the lower left. The maximum NRCS of the scattered signal is ~ -3 dB and the minimum in the shaded area is ~ -30 dB.

and

$$\sigma_{\text{vol}} = \int_0^{\infty} \eta[x(z)] e^{-2 \int_z^{\infty} k[x'(z')] dz' / \cos \theta} dz, \quad (1c)$$

where η (km^{-1}) is the radar reflectivity (or volume-scattering coefficient) and k (km^{-1}) is the extinction coefficient. The scattering volume occurs within a pulse oriented perpendicular to the direction of propagation.

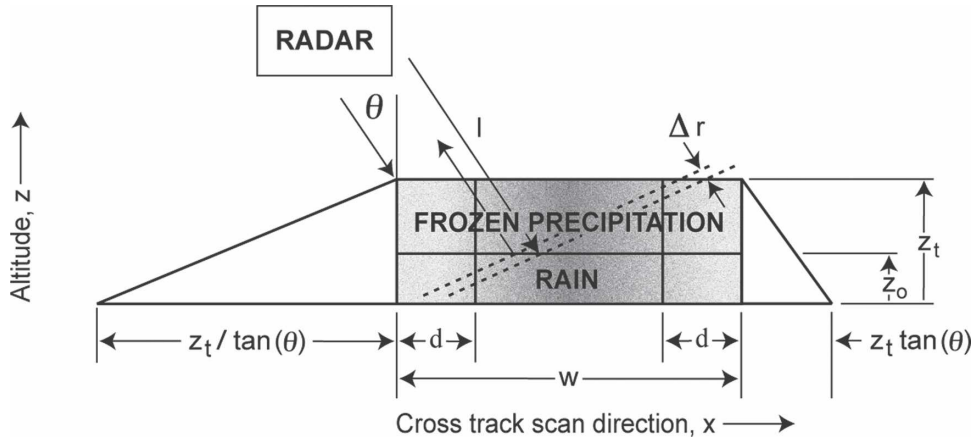


FIG. 2. Schematic view of the model used to compute the NRCS from a horizontally tapered two-layer precipitating cloud.

The average backscatter cross-section σ^0 for vertically polarized radiation incident on land at $\sim 30^\circ$ is about -7 dB (Oh et al. 1992). The appendix presents a detailed derivation of Eq. (1) from conventional SAR and radar meteorology definitions of σ^0 , k , and η .

Although various hydrometeors may occur in precipitating clouds, and these contribute differently to η and k , we confined our attention only to rain and snow. We can represent η through the effective (or equivalent) reflectivity factor Z_e :

$$\eta = \frac{\pi^5 |K|^2}{\lambda^4} Z_e, \tag{2}$$

where $\lambda = 3.1$ cm is the wavelength at which the X-SAR operates, and $|K|^2 = 0.93$ is a function of the refractive index of water where we neglect the effect of temperature. Effective reflectivity factors, Z_e ($\text{mm}^6 \text{m}^{-3}$), have been widely cited in the literature.

b. Electromagnetic properties of hydrometeors

Numerous power-law relationships between Z_e ($\text{mm}^6 \text{m}^{-3}$), k (km^{-1}), and R (mm h^{-1}) have been determined both theoretically and experimentally. Thus, by adopting a power-law relation, we can express

$$Z_e = aR^b \tag{3a}$$

and

$$k = c_1 R^{d_1} + c_2 R^{d_2}. \tag{3b}$$

Table 2 provides the constants used in Eq. (3). We assumed that the frozen hydrometeors were only snow to keep the analysis simple. As is the case for conventional radar measurements of precipitation, if the assumed constants in Eq. (3) differ from those applicable

to the case under consideration, the retrieved R will be degraded accordingly.

4. Precipitation spatial distribution models

The NRCS computations employed 2D precipitation distributions, $R(x, z)$, that varied with height z and along the scan direction x . A simple factorization with respect to the x and z axes was assumed to represent the 2D model as follows:

$$R(x, z) = H(x)V(z), \tag{4}$$

where $H(x)$ is a dimensionless horizontal weighting factor with a width w and a shape parameter d (see Fig. 2), and $V(z)$ is the precipitation rate vertical profile at the center of symmetric distributions.

a. Vertical rainfall rate profile

The vertical rainfall rate profiles were based on isopleths of equal probabilities of occurrence obtained from contoured frequency by altitude diagrams (CFAD; Yuter and Houze 1995). An analytic approximation was fitted to those contours:

$$V(z) = V(0) \left[0.85 + 0.15 \left(\frac{z_0 - z}{z_0} \right)^{0.62} \right] \text{ for } 0 \leq z \leq z_0 \tag{5a}$$

TABLE 2. Summary of constants appearing in Eqs. (3a) and (3b). Equation (3a) for rain is derived from Sekhon and Srivastava (1971) and for snow is derived from Ulaby et al. [1981, p. 329, Eq. (5.135c)]. Equation (3b) for rain is derived from Ulaby et al. (1981, p. 321, Table 5.7) and for snow is derived from Ulaby et al. [1981, p. 327, Eq. (5.131)].

	a	b	c_1	d_1	c_2	d_2
Rain	300	1.35	2.6×10^{-3}	1.11	0	0
Snow	182	1.6	5.6×10^{-3}	1.6	1.23×10^{-4}	1

and

$$V(z) = V(z_0) \left(\frac{z_t - z}{z_t - z_0} \right)^p \quad \text{for } z_0 \leq z \leq z_t, \quad (5b)$$

where z_0 and z_t are the heights of the freezing level and the top of the frozen precipitation, respectively. These heights can be obtained from climatology or from tem-

perature soundings. The parameter p defines the rate at which the frozen hydrometeor equivalent rainfall rate diminished with height.

b. Horizontal rainfall rate distribution

The dimensionless horizontal weighting factor $H(x)$ was generalized to vary along the scan line direction with a trapezoidal distribution:

$$H(x) \begin{cases} 0 & 0 \leq x \leq [z_t/\tan(\theta)] \\ x/d - z_t/[d \tan(\theta)] & [z_t/\tan(\theta)] \leq x \leq d + [z_t/\tan(\theta)] \\ 1 & \text{for } d + [z_t/\tan(\theta)] \leq x \leq w - d + [z_t/\tan(\theta)]. \\ (w - x)/d + z_t/[d \tan(\theta)] & w - d + [z_t/\tan(\theta)] \leq x \leq w + [z_t/\tan(\theta)] \\ 0 & w + [z_t/\tan(\theta)] \leq x \end{cases} \quad (6a)$$

The horizontal weighting factor $H(x)$ thus increases and decreases linearly and symmetrically with distance from the edges over a thickness d . In the extremes,

$d = 0$ corresponds to a rectangular distribution and $d = w/2$ describes a triangular distribution.

We also considered a twin column model with

$$H(x) \begin{cases} 0 & 0 \leq x \leq [z_t/\tan(\theta)] \\ 1 & [z_t/\tan(\theta)] \leq x \leq d + [z_t/\tan(\theta)] \\ 0 & \text{for } d + [z_t/\tan(\theta)] \leq x \leq w - d + [z_t/\tan(\theta)]. \\ 1 & w - d + [z_t/\tan(\theta)] \leq x \leq w + [z_t/\tan(\theta)] \\ 0 & w + [z_t/\tan(\theta)] \leq x \end{cases} \quad (6b)$$

c. Effect of model parameters on the NRCSs

The effect of varying $V(z)$ is shown in Fig. 3, which presents 4 of the 18 rainfall profiles considered in this study. The models assumed that the freezing heights were $z_0 = 4.65$ km. Melting layers were neglected. The tops of the snow layer were $z_t = 13$ km. The viewing angle θ in all subsequent computations is 30° . The horizontal weighting factors were assumed to be 6-km-wide rectangular distributions with $d = 0$. The profiles included a case based on TRMM PR measurements of a reflectivity profile with a ~ 57 -dBZ reflectivity factor [$V(0) = 150 \text{ mm h}^{-1}$ and $p = 0.32$] observed during the Indian monsoon by Houze et al. (2007). Two other profiles show a comparison of heavy and light snowfall distributions with a common surface rainfall rate [$V(0) = 96 \text{ mm h}^{-1}$ and $p = 0.08$ and 1.85 , respectively]. A case with light surface rainfall and modest snowfall [$V(0) = 32 \text{ mm h}^{-1}$ and $p = 1.85$] is also shown.

Figure 4 shows the NRCS scans that were derived from the profiles shown in Fig. 3. Note that a plume of NRCS > -7 dB rises gradually from the left edge of the scan line ($x = 0$) and remains above the background value to a range of 24 km. Because this increase is

gradual and because noise may obscure that rise, we will employ the location $x_0 \sim 23$ km as a reference point, where $x_0 \sim z_t/\tan(\theta)$ for $z_t = 13$ km and $\theta = 30^\circ$. A precipitous reduction in all of the NRCSs occurs at x_0 so that it can be used as a robust reference in a retrieval algorithm. The distance between x_0 and the location of the minimum value of the NRCS, x_{\min} , appears to be comparable to w , the width of the precipitation for rectangular distributions. The shaded area identifies where the rainfall occurred.

The mean value of the difference between the cross section and the background (-7 dB) to the left of x_0 is proportional to the mean snowfall rate above z_0 . The differences between the NRCS values to the right of x_0 and the background appear to be proportional to the rainfall rates at the surface.

Figure 5 compares the effect of triangular, rectangular, and twin column $H(x)$ horizontal distributions on three NRCS scans. For a rectangular distribution, Eq. (6a) with $d = 0$, the slope of the NRCS within 1.5 km to the right of x_0 diminishes markedly at ~ 20 km. The NRCS then diminishes at a lesser rate as one moves to the right toward x_{\min} , the location of the minimum NRCS value. For a triangular distribution, Eq. (6a)

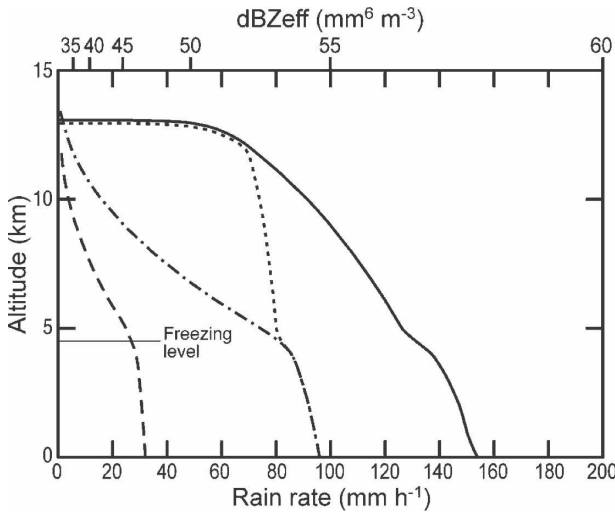


FIG. 3. Four examples of vertical profiles of rain rates, $V(z)$ (mm h^{-1}), used to compute the NRCS in Fig. 4. Curve 1 (dashed) is a profile with 32 mm h^{-1} surface rainfall and light snow content, curve 2 (dashed-dotted) is a profile with surface rainfall of 96 mm h^{-1} and modest snow content, and curve 3 (dotted) has the same liquid rain rate as curve 2 but with more snow. Curve 4 (solid line) is derived from a PR measurement over an Indian mesoscale convective complex that exceeded 40 dB to heights of $\sim 14 \text{ km}$ (Houze et al. 2007).

with $d = w/2$, the slope diminishes gradually near x_0 and then it diminishes more rapidly as one moves to the right toward x_{min} . The twin column case Eq. (6b) displays a clearly identifiable double dip.

5. Precipitation distribution retrieval algorithm

We now present an exploratory algorithm to retrieve the $\hat{V}(0)$, \hat{p} , \hat{w} , and \hat{d} of model rainfall rate distributions from NRCS scans. (Retrieved quantities are designated with circumflexes.) The values of θ , z_r , and z_0 are assumed known. Equation (1) shows that the NRCS consists of integrals of Z_e and k . As in the retrieval of rainfall rates from microwave radiometric measurements, the information derived from NRCS data can thus only provide integral constraints on a priori models or cloud-resolving model output. This exploratory retrieval algorithm for $R(x, z)$ seeks the parameters described in section 4 from several features of the NRCSs.

a. Determination of the crossing node \hat{x}_0

The value of \hat{x}_0 was found by taking a running mean over $n = 5$ sample values of the NRCS at a resolution of 250 m. Standard deviations of those five values were also computed. (Five samples were considered to minimize random noise that might exist in a single value.) If

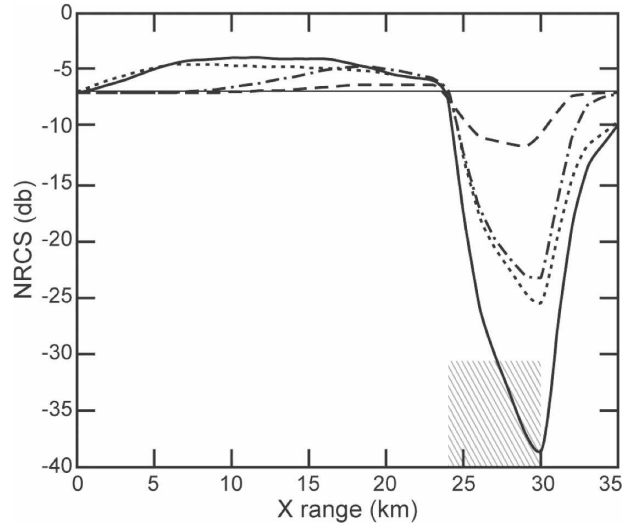


FIG. 4. Profiles of NRCS computed from the profiles shown in Fig. 3. The curves are designated as those shown in Fig. 3. The shaded area identifies the location of the 6-km-wide rectangular precipitation distribution.

the sixth value of the NRCS was less than the running mean of the $n = 5$ preceding points by more than three standard deviations, then that point was identified as \hat{x}_0 . This algorithm can be written as

$$\hat{x}_0 = x \text{ for } \sigma_{\text{SAR}}(x) < \{ \text{AVG}_n(\sigma_{\text{SAR}}) - 3\text{RMS}_n[\sigma_{\text{SAR}} - \text{AVG}_n(\sigma_{\text{SAR}})] \}, \tag{7}$$

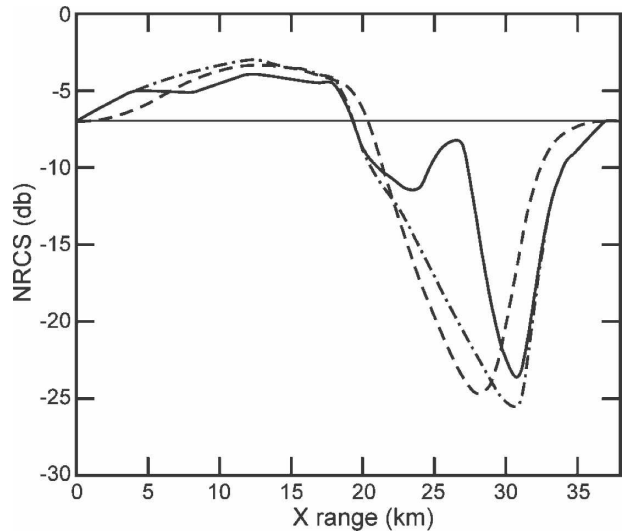


FIG. 5. An NRCS scan for a 12-km-wide rectangular precipitation distribution ($d = 0 \text{ km}$) with a 96 mm h^{-1} surface rainfall rate (dashed curve), an NRCS scan for a 12-km-wide triangular precipitation distribution ($d = 6 \text{ km}$) with a peak surface rainfall rate of 150 mm h^{-1} (dashed-dotted curve), and an NRCS scan from twin rectangular columns 4 km wide separated by 4 km ($d = 4 \text{ km}$) with a 96 mm h^{-1} maximum surface rainfall rate (solid line curve).

where x is the current cross-track position, whereas AVG_n and RMS_n are the average and root-mean-square values over n samples preceding the x position, respectively. The choice of $n = 5$ might depend on the X-SAR resolution and data processing. The values of \hat{x}_0 in the NRCS scans presented in Figs. 4 and 5 are ~ 24 and ~ 20 km, respectively.

b. Determination of the shape of the horizontal precipitation distribution

Inspection of Eq. (1) suggests that if one neglects scattering by frozen hydrometeors and only considers attenuation by rain, then the NRCS near the leading edge of the precipitation is

$$\sigma_{\text{srf}} \approx \sigma^0 e^{-2 \int_{z_t/\tan\theta}^x k(x') dx' / \sin(\theta)} \quad (8a)$$

for $z_t/\tan(\theta) \leq x \leq z_t [1/\tan(\theta) + \tan(\theta)]$. Thus

$$\langle \hat{V}_{\text{rain}}(0) \rangle_i \frac{d \ln(\sigma_{\text{srf}})}{dx} \approx \frac{-2k(x)}{\sin(\theta)} \quad (8b)$$

and taking the differences between derivatives of the NRCS at two locations where $x > \hat{x}_0$, then

$$k(\hat{x}_1) - k(\hat{x}_2) \approx \frac{\sin(\theta)}{2} \left\{ \frac{d \ln[\sigma_{\text{srf}}(\hat{x}_2)]}{dx} - \frac{d \ln[\sigma_{\text{srf}}(\hat{x}_1)]}{dx} \right\}. \quad (8c)$$

The $\hat{x}_1 = \hat{x}_0 + 1.5$ km provides a convenient reference. The $\hat{x}_2 = (\hat{x}_0 + \hat{x}_{\text{min}})/2$ is also easy to define once \hat{x}_{min} is identified. The minimum NRCS at \hat{x}_{min} was found by taking a running mean of five 250-m values of the NRCS centered on the nominal scan position under consideration. Taking the difference between the sample sets on either side of the nominal scan position yielded the first-order D^1 and second-order D^2 incremental ratios of the smoothed NRCS $AVG_n(\sigma^0)$:

$$D^1 = \frac{\Delta AVG_n(\sigma^0)}{\Delta x} \quad \text{and} \quad D^2 = \frac{\Delta^2 AVG_n(\sigma^0)}{\Delta x^2}, \quad (8d)$$

where Δx are the x increments. These numerical and second derivatives yielded a robust estimate of \hat{x}_{min} . Smoothed slopes defined in Eq. (8c) were then determined at \hat{x}_1 and \hat{x}_2 . Because the difference between the derivatives for a rectangular distribution of $H(x)$ is nearly zero, whereas that for a triangular distribution of $H(x)$ depends nearly linearly on x , a threshold for the difference between those slopes was empirically set to discriminate between triangular and rectangular distributions.

This procedure enabled the \hat{d}/\hat{w} ratios that characterized all 18 models of $H(x)$ to be correctly identified.

c. Determination of the width of the precipitation

The locations of \hat{x}_0 and \hat{x}_{min} were also used to retrieve the width \hat{w} of the precipitation cells. For rectangular and twin column distributions

$$\hat{w} = 0.97(\hat{x}_{\text{min}} - \hat{x}_0), \quad (9a)$$

and for triangular distributions

$$\hat{w} = 1.61(\hat{x}_{\text{min}} - \hat{x}_0)^{0.93}. \quad (9b)$$

Equations (9a) and (9b) yielded an RMS value of the relative error $(w - \hat{w})/w$ equal to 0.08 for the 18 cases that were considered.

d. Determination of the average rain vertical profile

Having estimated the parameters \hat{d} and \hat{w} of $H(x)$, the average precipitation rate vertical distribution $\langle V(z) \rangle$ can be obtained by integrating the horizontal weighting function from Eq. (4) over the x domain:

$$\langle V(z) \rangle = \frac{V(z)}{\hat{w}} \int_0^{\hat{w}} H(x) dx \quad \text{for} \quad 0 \leq z \leq z_t. \quad (10)$$

By determining the vertical profile of the average rainfall rate for $0 \leq z < z_0$, the averaged profile $\langle V_{\text{rain}}(z) \rangle$ can be empirically related to the averaged surface rainfall rate $\langle V_{\text{rain}}(0) \rangle$ from Eq. (5a).

The NRCS response to the average surface rainfall rate is related mainly to the area between the background σ^0 and the measured NRCS (dB). However, a correction must be made to account for the scattering within the snow layer and the width of the precipitation. The retrieved average surface rainfall rate (mm h^{-1}) was found by a linear regression to be

$$\begin{aligned} \langle \hat{V}_{\text{rain}}(0) \rangle = & 1.13 \int_{\hat{x}_0}^{\hat{x}_{\text{max}}} [dB\sigma^0(x_{\text{max}}) - dB\sigma_{\text{SAR}}(x)] dx \\ & - 21.62 \int_0^{\hat{x}_0} [\sigma_{\text{SAR}}(x) - \sigma^0(0)] dx - 2.58\hat{w} + 23.30, \end{aligned} \quad (11)$$

where the first integral is proportional to the difference of the logarithm of the background and that of the NRCS, that is, over the region $\hat{x}_0 \leq x \leq \hat{x}_{\text{max}}$. This is a region where the σ_{SAR} is strongly attenuated by rain. The second integral is a function of the difference between the background and the precipitation cross section where the scattering signature of the snowfall is dominant. The reflectivity of the snowfall hydrometeors is more closely related to σ_{SAR} rather than to $dB\sigma_{\text{SAR}}$. The last term accounts for the dependence on the width of $H(x)$. The units of the terms are millimeters per hour, mm h^{-1} (dB km) $^{-1}$, mm (h km) $^{-1}$, and

mm (h km⁻¹), respectively. The values of these terms are only appropriate for $\theta = 30^\circ$ and the values of z_0 and z_t employed in the models. They need to be modified for other model values.

e. Determination of the average vertical snow profile

In Eq. (5b), the snowfall rate profile $V_{\text{snow}}(z)$ diminishes with height for $z_0 \leq z < z_t$ at a rate determined by the parameter p and the height at which the snow no longer occurs z_t .

Integrating Eq. (5b) between $z_0 \leq z \leq z_t$ yields the average snowfall rate $\langle V_{\text{snow}} \rangle$:

$$\begin{aligned} \langle V_{\text{snow}}(z) \rangle &= \frac{1}{w(z_t - z_0)} \\ &\times \int_{z_0}^{z_t} \int_{z_t/\tan\theta}^{(z_t/\tan\theta) + \hat{w}} H(x) V_{\text{snow}}(z) dx dz \end{aligned} \tag{12}$$

from which it follows that

$$\hat{p} = \frac{\langle \hat{V}_{\text{rain}}(z_0) \rangle}{\langle \hat{V}_{\text{snow}}(z) \rangle} - 1, \tag{13a}$$

where $\langle \hat{V}_{\text{snow}}(z_0) \rangle = \langle \hat{V}_{\text{rain}}(z_0) \rangle$ is due to the continuity of the precipitation profile. The average snowfall rate can be derived from the NRCS using the empirical relationship derived from a regression analysis of available simulation models:

$$\langle \hat{V}_{\text{snow}}(z_0) \rangle = \frac{183 \left\{ \int_0^{x_0} [\sigma_{\text{SAR}}(x) - \sigma_{\text{SAR}}(0)] dx \right\}^{0.94}}{\hat{w}^{1.04}}, \tag{13b}$$

where the constant is in units of km^{0.08} mm h⁻¹. Again, the values of the constants are appropriate *only* for $\theta = 30^\circ$ and the values of z_0 and z_t employed in these models.

The retrieved top of the snow layer is

$$\hat{z}_t = z_0 + (\hat{p} + 2)\langle \hat{z} - z_0 \rangle. \tag{14a}$$

The term on the right is the centroid of the snowfall rate profile measured above the freezing level:

$$\langle \hat{z} - z_0 \rangle = \frac{\int_{z_0}^{z_t} (z - z_0) V_{\text{snow}}(z) dz}{\int_{z_0}^{z_t} V_{\text{snow}}(z) dz}. \tag{14b}$$

This centroid can be derived from the centroid of the NRCS measured to the left of x_0 :

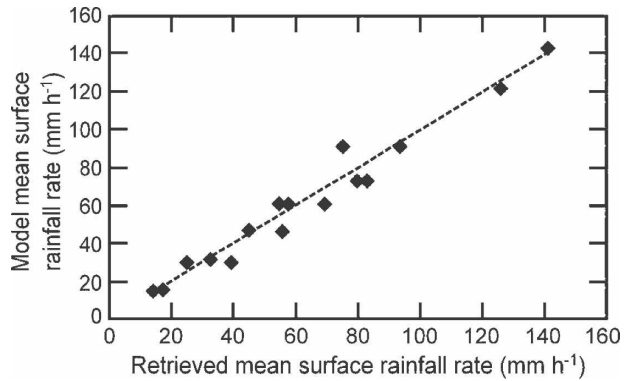


FIG. 6. The average surface rainfall rate retrieved from the application of Eq. (11) to the computed NRCS compared with the input average surface rainfall rate of the model.

$$\langle \langle \hat{x} - x_0 \rangle \rangle = \frac{\int_0^{x_0} (x - x_0) [\sigma_{\text{SAR}}(x) - \sigma_{\text{SAR}}(0)] dx}{\int_0^{x_0} [\sigma_{\text{SAR}}(x) - \sigma_{\text{SAR}}(0)] dx}. \tag{14c}$$

The centroid of the snowfall rate distribution Eq. (14b) can be empirically related to the centroid derived from the NRCS Eq. (14c) by

$$\langle \langle \hat{z} - z_0 \rangle \rangle = \begin{cases} 0.38 \langle \langle \hat{x} - x_0 \rangle \rangle \\ 0.43 \langle \langle \hat{x} - x_0 \rangle \rangle \end{cases} \tag{14d}$$

for rectangular distributions (above) and triangular distributions (below).

6. Retrieval results

We will now present a comparison between the model and retrieved precipitation profiles.

Figure 6 presents a comparison between the model, $\langle V_{\text{rain}}(0) \rangle$, and the retrieved, $\langle \hat{V}_{\text{rain}}(0) \rangle$, values of the average surface rainfall rate from Eq. (11). The $\text{RMS}_n(0)$ relative error of the surface rain rate is

$$\text{RMS}_n(z) = \sqrt{\frac{1}{n} \sum_{i=1}^n \left[\frac{\langle \hat{V}(z) \rangle_i - \langle V(z) \rangle_i}{\langle V_{\text{rain}}(0) \rangle_i} \right]^2}. \tag{15}$$

For $z = 0$, the $\text{RMS}_n(0)$ is about 0.10 for the $n = 18$ cases that were considered. By contrast, the model population had a mean $\langle V_{\text{rain}}(0) \rangle \sim 65 \text{ mm h}^{-1}$ with a 37 mm h^{-1} standard deviation so that $\text{RMS}_n(0) \sim 0.6$ for the model population as a whole.

The precipitation profiles were normalized with respect to their average surface rainfall rates, $\langle \hat{V}(z) \rangle / \langle V_{\text{rain}}(0) \rangle$, to permit a compact comparison among the various profiles. Figure 7 shows the root-mean-square deviation between the model and retrieved normalized profiles for $n = 18$. Because these profiles are normal-

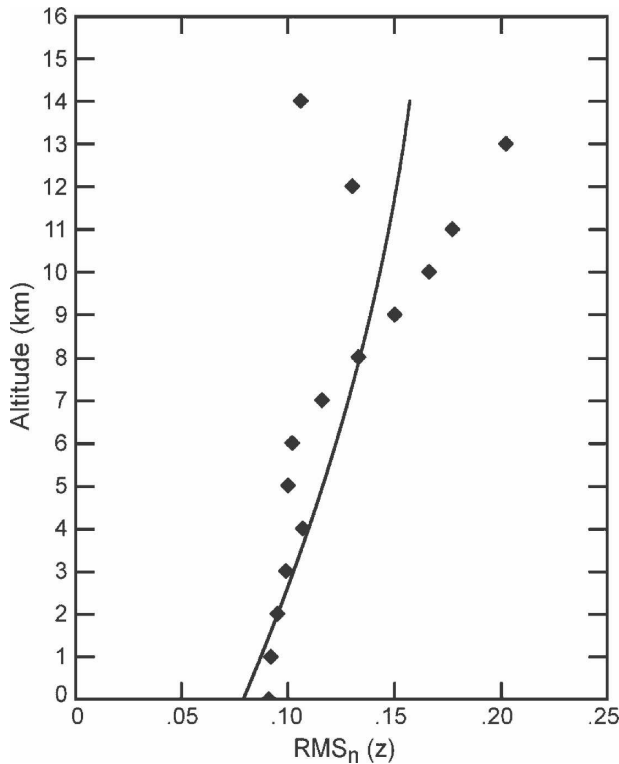


FIG. 7. Vertical profile of the $RMS_n(z)$ of the difference between the normalized model and the retrieved distributions of rainfall rates defined by Eq. (15).

ized to $\langle V_{rain}(0) \rangle_i$ for each of the i profiles, the probable uncertainty in $\langle \hat{V}_{rain}(0) \rangle_i$ is $\sim 0.1 \langle V_{rain}(0) \rangle_i$. That uncertainty increases monotonically to $\sim 0.2 \langle \hat{V}_{rain}(0) \rangle$ at 12 km. Although that may not appear to be large, it can yield an error that is greater than $\langle V_{snow}(z) \rangle_i$ at high altitudes.

Figure 8 presents two rainfall distributions, $R(x, z)$, retrieved from NRCS data along the transects A–A' and B–B' shown in Fig. 1. Unfortunately, no independent measurements were available to validate the retrieved distributions. However, those distributions appear qualitatively consistent with PR radar measurements over the Indian subcontinent found by Houze et al. (2007).

7. Discussion of results and conclusions

The most striking aspect of NRCS imagery of convective storms over land is the enhancement of the NRCS on the illuminated side of the precipitating cells and the attenuation on the “shadowed” sides shown in Fig. 1. The measured NRCS at the leading edge is the sum of the scattering from the surface plus that from the snow. As the radar footprint scans into the rain itself, the surface scattering is attenuated by the rain

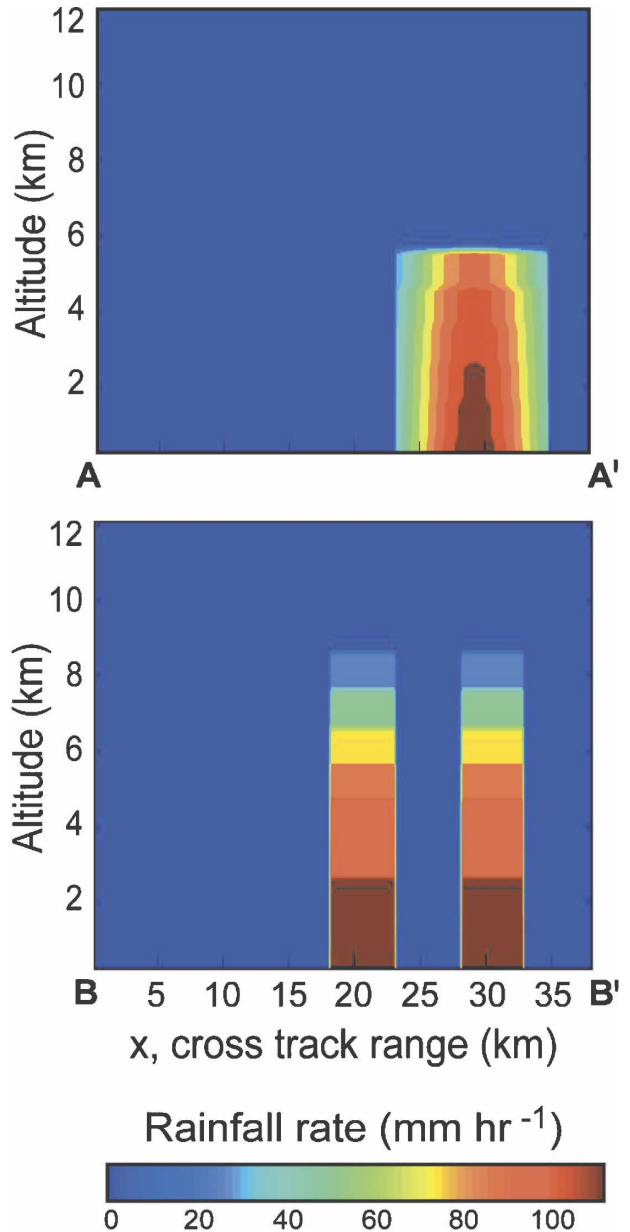


FIG. 8. Vertical cross sections of rainfall rates retrieved along transects A–A' and B–B' shown in Fig. 1.

and the additional backscattering by the rain is also attenuated. Finally, as the scan approaches the farside of the rain, the NRCS increases as the attenuation path through the rain diminishes. A two-layer model consisting of snow and rain in a cloud, shown in Fig. 2, permitted us to account for some of the features of the NRCS shown in Fig. 1. Figure 3 showed vertical profiles at the centers of the modeled precipitation. Figure 4 showed the NRCS from those horizontally uniform cloud models with rectangular distributions. The NRCS values that exceeded the background values depended

mainly on the vertical distribution of the frozen hydrometeors $V(z)$. The part of the NRCS that was less than the background value depended mainly on attenuation by the rainfall. Figure 5 compared the NRCS for precipitation distributions with differing horizontal weighting functions. Differences in the appearances of these NRCS scans illustrate that information regarding the horizontal distribution of precipitation could also be derived from NRCS scans.

It was possible to retrieve features of the horizontal weighting functions of the precipitation distributions. The shapes of the horizontal distributions $H(x)$ were identified by an ad hoc relationship between the slopes of the NRCS. Figure 4 showed that the range from the start of the diminution to the minimum value of the NRCS was a measure of the width of the precipitating column. Computing the average value of the reduction of the NRCS from the background provided a measure of the average liquid rainfall below the freezing height. The curves representing rectangular and triangular distributions with equal average NRCS were shown to have nearly equal average surface rainfall rates.

A more mathematically elegant rainfall retrieval algorithm based on an analysis of spaceborne real aperture radar measurements by Pichugin and Spiridonov (1991) was subsequently developed by Marzano and Weinman (2008). These studies transformed the radar equation into a Volterra integral equation of the second kind. Unlike the earlier study, the latter work could accommodate profiles consisting of rain and snow (Press et al. 2007). Frozen hydrometeors were neglected in that analysis. Our exploration of the Volterra integral equation approach will be presented in a subsequent work (Marzano and Weinman 2008).

Parameters describing the vertical distribution $V(z)$ of precipitation were also retrieved from the NRCSs: these included the average surface rainfall rate, the height of the top of the frozen hydrometeors, and a parameter describing the shape of the diminution of the snowfall rate as a function of height. It is evident from Fig. 4 that the horizontal extent of the region with an NRCS that was greater than the background value (-7 dB) depended on the vertical distribution of the frozen hydrometeors. The value of that enhanced NRCS averaged over that distance is proportional to the average snowfall rate and the centroid.

Figure 7 showed that the $\text{RMS}_n(z)$ of the normalized rainfall rate profiles was between 0.1 and 0.2. The ratio of the standard deviation to the mean of the *entire* model population was ~ 0.6 . The retrieval thus represented a significant improvement over chance.

Inspection of Fig. 1 showed that the background NRCS was $\sigma^0 \sim -7 \pm 1$ dB. The ± 1 -dB variation may

limit the accuracy of rainfall rates that can be derived from NRCS measurements at X band. Model runs for 6-km-wide rectangular clouds with rainfall rates of 16 mm h^{-1} produced 2-dB NRCS departure from the background. This may be indicative of the rainfall detection limit of X-SAR measurements. (That rainfall rate may correspond to an averaged rainfall rate of $\sim 0.8 \text{ mm h}^{-1}$ that would be observed within the $\sim 600 \text{ km}^2$ footprints of microwave radiometers.)

Figure 8 presented the results of a retrieval based on the moments described in section 5. While these results appear plausible, coincident measurements of X-SAR and aircraft-borne or ground-based radars will be needed to evaluate the validity of rainfall distributions derived from X-SAR measurements.

This study assumed that the Z_e - k relationship was known for the hydrometeors in the cloud, as is the case for all simple radar backscattering precipitation measurements. The height of the freezing level was also assumed to be known as was the cross section of the background. Considering all of the components in a precipitating cloud, and that the NRCS depends on integrals of Z_e and k , it will be necessary to move beyond the present analysis into a Bayesian retrieval algorithm, such as that of Marzano et al. (1999). Such an algorithm will surely incorporate information from cloud-resolving models similar to those used to retrieve precipitation from microwave radiometric measurements (e.g., Kummerow and Giglio 1994; Tassa et al. 2006). Some of the considerations presented in this study can, however, provide guidance for the development of such a retrieval algorithm.

Acknowledgments. Discussions with Drs. Alberto Mugnai, ISAC National Research Council, Rome, Italy, and Susanne Lehner of DLR were helpful in formulating some of the ideas presented in this paper. Messrs. G. Poccia and R. Cantelmi are acknowledged for their contribution to the X-SAR data numerical analysis. X-SAR digital data were kindly provided by Dr. F. Nirchio of ASI, Matera, Italy. The graphic assistance of Ms. Beth Tully is also acknowledged. Part of this research was funded by NASA Grant NAG5-9668 under the oversight of Drs. Gail S. Jackson and Ramesh Kakar and we thank them for their support.

APPENDIX

Derivation of the Normalized Radar Cross Section due to Rainfall

There are several expressions of NRCS due to rainfall available in the literature (e.g., Pichugin and Spiri-

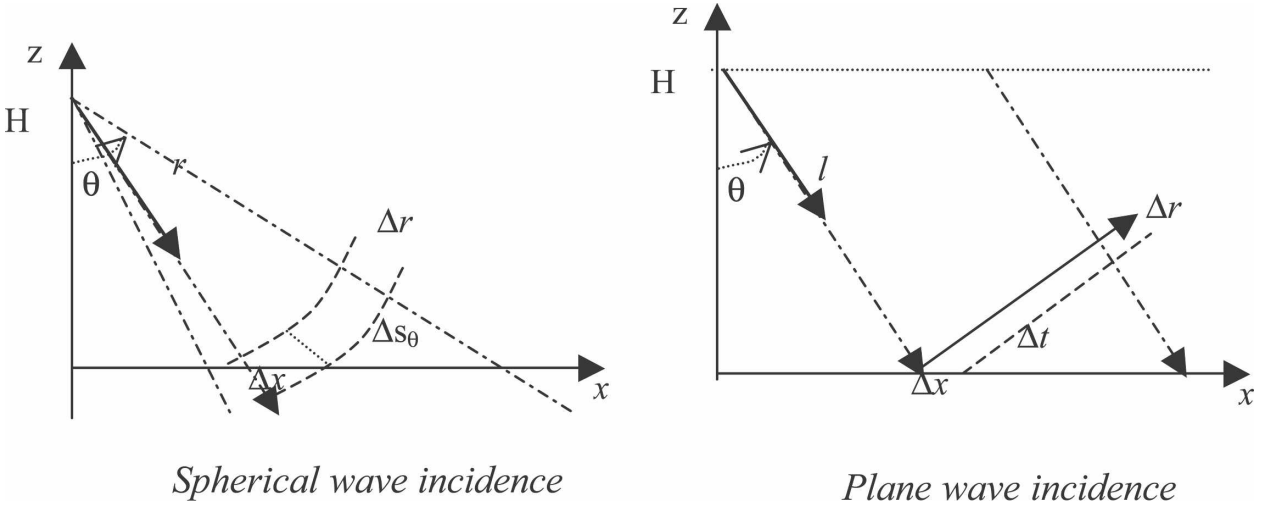


FIG. A1. Cross-track geometry for an X-SAR NRCS model; (left) spherical wave incidence and (right) plane-wave incidence. The main parameters used in the appendix are also indicated.

donov 1991; Moore et al. 1997; Melsheimer et al. 1998). Most use simplified formulas that consider homogeneous rain slabs subjected to plane-wave incidence. This appendix will establish a general theoretical framework to derive the NRCS from an analytical model valid for inhomogeneous rain clouds and spherical wave incidence.

From the radar equation for single scattering in a spherical coordinate system centered at the radar antenna at height H (see left panel of Fig. A1), the received power W_R is expressed by

$$\begin{aligned}
 W_R(r, \theta, \varphi) &= \frac{\lambda^2 G_M^2}{(4\pi)^3} U_n^2(\theta, \varphi) \frac{\sigma_b(r, \theta, \varphi)}{r^4} L^2(r, \theta, \varphi) \\
 &= CU_n(\Omega) \frac{\sigma_b(r, \theta, \varphi)}{r^4} L^2(r, \theta, \varphi), \quad (A1)
 \end{aligned}$$

where C is the instrumental constant (depending on antenna maximum gain G_M and wavelength λ), U_n is the one-way normalized antenna power diagram with θ and φ , the zenith and azimuth angles, and r is the range. The *backscattering radar cross section* is defined by

$$\sigma_b(r, \theta, \varphi) = 4\pi r^2 \frac{P_s(r, \theta, \varphi)}{P_i(r, \theta_i, \varphi_i)}, \quad (A2)$$

where P_s is the backscattered power density (or Poynting vector amplitude) and P_i is the incident power density along the direction (θ_i, φ_i) . The *one-way attenuation factor* L along an inhomogeneous extinguishing medium is L so that

$$L^2(r, \theta, \varphi) = e^{-2 \int_0^r k(r') dr'}, \quad (A3)$$

where k is the extinction power coefficient.

For a pulsed radar the range resolution is given by $\Delta r = c\Delta t/2$, where Δt is the pulse duration and c is the speed of light. We should distinguish between the *surface area* along the *slant range* A_r and its *horizontal projection* A , as displayed in Fig. A1 in a schematic way, defined as

$$A_r = \Delta r \Delta s_\varphi \quad \text{and} \quad A = \Delta x \Delta s_\varphi \cong \frac{\Delta r}{\sin \theta} \Delta y_a = \frac{A_r}{\sin \theta}, \quad (A4)$$

where Δx is the cross-track resolution along x and Δs_φ is an elementary arc along φ (in the along-track plane r - y). Note that the slant area A_r is *always defined*, whereas the horizontal area A may depend on the *local surface slopes*.

It is customary to define the NRCS σ^0 for bare soil or sea surfaces as

$$\sigma^0 = \frac{\sigma_b}{A} = \frac{\sigma_b A_r}{A_r A} = \beta^0 \sin \theta, \quad (A5)$$

where β^0 is the slant NRCS. In a similar way, when the e.m. interaction is volumetric (as for rainfall or vegetation), it is common to define the *radar reflectivity* η as

$$\eta = \frac{\sigma_b}{V_r} = \frac{\sigma_b}{\Delta s_\theta \Delta s_\varphi \Delta r}, \quad (A6)$$

where Δs_θ is the elementary arc along θ (in the cross-track plane z - x). Note that η is homogeneous with β^0 and not with σ^0 , as it is normalized to the slant volume.

Considering the surface-scattering response, the radar equation can be integrated along the illuminated slant area to obtain the average echo power:

$$\begin{aligned}\bar{W}_{R\text{srf}}(r) &= C \int_{A_r} \frac{U_n^2(\theta, \varphi) \sigma_b(r, \theta, \varphi)}{r^4} dA_r L^2(r, \theta, \varphi) \\ &\cong C \int_{\Delta r} \int_{\Delta s_\varphi} \frac{U_n^2(\theta, \varphi)}{r^4} \beta^0(r, \theta, \varphi) L^2(r, \theta, \varphi) ds_\varphi dr.\end{aligned}\quad (\text{A7})$$

Assuming that the slant NCRS β^0 and the extinction coefficient k are weakly dependent on φ , and noting that for surface scattering at θ may be considered almost fixed, we can approximate the previous equation by

$$\bar{W}_{R\text{vol}}(r) = C \int_{V_r} \frac{U_n^2(\theta, \varphi) \sigma_b(r, \theta, \varphi)}{r^4} dV_r L^2(r, \theta, \varphi) \cong C \int_{\Delta r} \int_{\Delta s_\varphi} \int_{\Delta s_\theta} \frac{U_n^2(\theta, \varphi)}{r^4} \eta(r, \theta, \varphi) L^2(r, \theta, \varphi) ds_\theta ds_\varphi dr, \quad (\text{A9})$$

where Δr is the resolution interval at range r where V_r is defined. Again the reflectivity η and the extinction coefficient k can be assumed to be weakly dependent on φ , but for volume scattering we need to con-

$$\begin{aligned}\bar{W}_{R\text{srf}}(r) &\cong C \left[\int_{\Delta r} \int_{\Delta s_\varphi} \frac{U_n^2(\theta, \varphi)}{r^2} ds_\varphi dr \right] \frac{\beta^0(r) L^2(r)}{r^2} \\ &= \frac{C_u \sigma^0(r)}{r^2 \sin \theta} L^2(r),\end{aligned}\quad (\text{A8})$$

where C_u is a new constant including the antenna diagram integration and r is such that $z = 0$ (i.e., the back-scattering is from surface targets).

Because the volume can be anywhere within the range interval, the radar equation can be integrated over the *illuminated volume* V_r to obtain the average echo power following the similar steps as before:

sider the inhomogeneity along θ as the volume V_r may extend up to the tropopause. Thus the previous equation becomes

$$\bar{W}_{R\text{vol}}(r) \cong C \left[\int_{\Delta r} \int_{\Delta s_\varphi} \frac{U_n^2(\theta, \varphi)}{r^2} ds_\varphi dr \right] \frac{1}{r^2} \int_{\Delta s_\theta} \eta(r, \theta) L^2(r, \theta) ds_\theta = \frac{C_u}{r^2} \int_{\Delta s_\theta} \eta(r, \theta) L^2(r, \theta) ds_\theta. \quad (\text{A10})$$

In terms of received echoes, the sum of the received average powers from surface and volume targets becomes

$$\begin{aligned}\bar{W}_{R\text{tot}}(r) &= \bar{W}_{R\text{srf}}(r) + \bar{W}_{R\text{vol}}(r) \\ &= \frac{C_u \sigma^0(r)}{r^2 \sin \theta} L^2(r) + \frac{C_u}{r^2} \int_{\Delta s_\theta} \eta(r, \theta) L^2(r, \theta) ds_\theta.\end{aligned}\quad (\text{A11})$$

To have a definition consistent with σ^0 , which is widely used in literature, a SAR *normalized radar cross section* σ_{SAR} can be defined as

$$\begin{aligned}\sigma_{\text{SAR}}(r) &\equiv \sin \theta \frac{r^2}{C_u} \bar{W}_{R\text{tot}} \\ &= \sin \theta \frac{r^2}{C_u} [\bar{W}_{R\text{srf}}(r) + \bar{W}_{R\text{vol}}(r)],\end{aligned}\quad (\text{A12})$$

which implies the following expression:

$$\begin{aligned}\sigma_{\text{SAR}}(r) &\equiv \sigma_{\text{srf}}(r) + \sigma_{\text{vol}}(r) \\ &= \sigma^0(r) L^2(r) + \sin \theta \int_{\Delta s_\theta} \eta(r, \theta) L^2(r, \theta) ds_\theta.\end{aligned}\quad (\text{A13})$$

To simplify the previous model, we can resort to plane-wave approximation as in Fig. A1 (right panel). To this aim we can define a rectilinear coordinate l - t in the cross-track plane such that l is the longitudinal coordinate along the plane-wave direction and t is the transverse coordinate with respect to l . The SAR returns will be now computed for each x position, which is the position of the incidence of each plane-wave direction on the surface. Thus, we can express Eq. (A13) as

$$\begin{aligned}\sigma_{\text{SAR}}(x) &\equiv \sigma_{\text{srf}}(x) + \sigma_{\text{vol}}(x) \\ &= \sigma^0(l) L^2(l) + \sin \theta \int_{\Delta t} \eta(l, t) L^2(l, t) dt,\end{aligned}\quad (\text{A14})$$

where Δt is the complete transverse path along t (see Fig. A1). Noting that $t = z/\sin \theta$, $l = x/\sin \theta$, and $H - z = l \cos \theta$ we can derive the explicit formula given in Eq. (1).

It is worth evaluating the error due the plane-wave geometry with respect to the spherical one. This error $\delta(t)$ can be approximated as $\delta(t) \cong t^2/(2l)$, where $t = z_r/\sin\theta$ and $l = H/\cos\theta$. Here, as before, z_r is the height of the rain cloud top and H is the satellite height. For $\theta = 30^\circ$, $z_r \cong 10$ km, and $H = 800$ km, the resulting $\delta(t) \cong 0.2$ km. This error is within an acceptable spatial resolution.

Last, a consideration on the along-track resolution should be pointed out. By neglecting the so-called range migration (i.e., error due to the spherical wave front incidence along track), we might approximate $\Delta s_\varphi \cong \Delta y$. It has been proved that, in the presence of rain, we can estimate $\Delta y \cong \sigma_v(2R/u_{\text{sat}})$, where σ_v is the hydrometeor velocity standard deviation, and R is the slant range from the satellite (Atlas and Moore 1987). By assuming $R = H/\cos\theta$ with H and θ as above, $u_{\text{sat}} = 7$ km s⁻¹ and $\sigma_v = 1$ m s⁻¹, we can estimate an along-track resolution of $\Delta y \cong 264$ m. This resolution is poorer than that achievable for a fixed target, a resolution that in a ScanSAR mode (e.g., see COSMO-SkyMed specifications) can be on the order of a few tens of meters. However, this degraded along-track resolution is still very high when compared with the resolution of spaceborne real aperture radars and microwave radiometers.

REFERENCES

- Atlas, D., and R. K. Moore, 1987: The measurement of precipitation with synthetic aperture radar. *J. Atmos. Oceanic Technol.*, **4**, 368–376.
- Bennartz, R., and G. W. Petty, 2001: The sensitivity of microwave remote sensing observations of precipitation to ice particle size distributions. *J. Appl. Meteor.*, **40**, 345–364.
- Buckreuss, S., W. Balzer, P. Muhlbauer, R. Werninghaus, and W. Pitz, 2003: The TerraSAR-X satellite project. *Proc. IEEE Int. Geoscience and Remote Sensing Symp. (IGARSS03)*, Toulouse, France, IEEE, 3096–3098.
- Caltagirone, F., G. Angino, F. Impagnatiello, A. Capuzi, S. Fagioli, and R. Leonardi, 2007: COSMO-SkyMed: An advanced dual system for Earth observation. *Proc. IEEE Int. Geoscience and Remote Sensing Symp. (IGARSS07)*, Barcelona, Spain, IEEE.
- Durden, S. L., Z. S. Haddad, A. Kitiyakara, and F. K. Li, 1998: Effects of nonuniform beam filling on rainfall retrieval for the TRMM precipitation radar. *J. Atmos. Oceanic Technol.*, **15**, 635–646.
- Houze, R. A., Jr., D. C. Wilton, and B. F. Smull, 2007: Monsoon convection in the Himalayan region as seen by the TRMM precipitation radar. *Quart. J. Roy. Meteor. Soc.*, **133**, 1389–1411.
- Jameson, A. R., F. Li, S. L. Durden, Z. S. Haddad, B. Holt, T. Fogarty, E. Im, and R. K. Moore, 1997: SIR-C/X-SAR observations of rainstorms. *Remote Sens. Environ.*, **59**, 267–279.
- Jordan, R. L., B. L. Huneycutt, and M. Werner, 1995: The SIR-C/X SAR synthetic aperture radar system. *IEEE Trans. Geosci. Remote Sens.*, **33**, 829–839.
- Kummerow, C., 1998: Beamfilling errors in passive microwave rainfall retrievals. *J. Appl. Meteor.*, **37**, 356–370.
- , and L. Giglio, 1994: A passive microwave technique for estimating rainfall and vertical structure information from space. Part I: Algorithm description. *J. Appl. Meteor.*, **33**, 3–18.
- , and Coauthors, 2000: The status of the Tropical Rainfall Measuring Mission (TRMM) after two years in orbit. *J. Appl. Meteor.*, **39**, 1965–1982.
- Marzano, F. S., and J. A. Weinman, 2008: Inversion of spaceborne X-band synthetic aperture radar measurements for precipitation remote sensing over land. *IEEE Trans. Geosci. Remote Sens.*, in press.
- , A. Mugnai, G. Panegrossi, N. Pierdicca, E. A. Smith, and J. Turk, 1999: Bayesian estimation of precipitating cloud parameters from combined measurements of spaceborne microwave radiometer and radar. *IEEE Trans. Geosci. Remote Sens.*, **37**, 596–613.
- Melshimer, C., M. Gade, and W. Alpers, 1998: Investigation of multifrequency/multipolarization radar signatures of rain cells derived from SIR-C/X-SAR data. *J. Geophys. Res.*, **103**, 18 867–18 884.
- Moore, R. K., A. Mogli, Y. Fang, B. Beh, and A. Ahamad, 1997: Rain measurement with SIR-C/X-SAR. *Remote Sens. Environ.*, **59**, 280–293.
- Oh, Y., K. Sarabandi, and F. T. Ulaby, 1992: An empirical model and an inversion technique for radar scattering from bare soil surfaces. *IEEE Trans. Geosci. Remote Sens.*, **30**, 370–381.
- Pichugin, A. P., and Yu. G. Spiridonov, 1991: The spatial distribution of rainfall intensity recovery from space radar images. *Sov. J. Remote Sens.*, **8**, 917–932.
- Press, W. H., S. A. Teukolsky, B. P. Flannery and W. T. Vetterling, 2007: *Numerical Recipes in C/C++*. 3rd ed. Cambridge University Press, CD-ROM.
- Schwerdt, M., D. Hounam, J.-L. Alvarez-Pères, and T. Molkenhuth, 2005: The calibration concept of TerraSAR-X: A multiple-mode, high-resolution SAR. *Can. J. Remote Sens.*, **31**, 30–36.
- Sekhon, R. S., and R. C. Srivastava, 1971: Doppler radar observations of drop size distributions in a thunderstorm. *J. Atmos. Sci.*, **28**, 983–994.
- Tassa, A., S. Di Michele, A. Mugnai, F. S. Marzano, P. Bauer, and J. P. V. Póiares Baptista, 2006: Modeling uncertainties for passive microwave precipitation retrieval: Evaluation of a case study. *IEEE Trans. Geosci. Remote Sens.*, **44**, 78–89.
- Ulaby, F. T., R. K. Moore, and A. K. Fung, 1981: *Microwave Remote Sensing Fundamentals and Radiometry*. Vol. I. *Microwave Remote Sensing: Active and Passive*, Artech House, 456 pp.
- Verdone, G. R., R. Viggiano, E. Lopinto, G. Millillo, L. Candela, N. Lombardi, and V. Giannini, 2002: Processing algorithms for COSMO-SkyMed SAR sensor. *Proc. IEEE Int. Geoscience and Remote Sensing Symp. (IGARSS02)*, Toronto, ON, Canada, IEEE, 2771–2774.
- Weber, M., and J. H€ermann, 2006: TerraSAR-X and TanDEM-X: Global mapping in 3D using radar. *Proc. Second Int. Workshop "The Future of Remote Sensing,"* Antwerp, Belgium, ISPRS Intercommission Working Group I/V Autonomous Navigation, 36–1/W44.
- Yuter, S. E., and R. A. Houze, 1995: Three-dimensional kinematic and microphysical evolution of Florida cumulonimbus. Part II: Frequency distributions of vertical velocity, reflectivity, and differential reflectivity. *Mon. Wea. Rev.*, **123**, 1941–1963.